

Research Article

An Inhomogeneous Cell-Based Smoothed Finite Element Method for Free Vibration Calculation of Functionally Graded Magnetoelastoelectric Structures

Yan Cai , Guangwei Meng , and Liming Zhou 

School of Mechanical Science and Engineering, Jilin University, Changchun 130025, China

Correspondence should be addressed to Liming Zhou; lmzhou@jlu.edu.cn

Received 27 October 2017; Revised 23 December 2017; Accepted 15 January 2018; Published 7 March 2018

Academic Editor: Marco Alfano

Copyright © 2018 Yan Cai et al. This is an open access article distributed under the Creative Commons Attribution License, which permits unrestricted use, distribution, and reproduction in any medium, provided the original work is properly cited.

To overcome the over stiffness and imprecise magnetoelastoelectric coupling effects of finite element method (FEM), we present an inhomogeneous cell-based smoothed FEM (ICS-FEM) of functionally graded magnetoelastoelectric (FGMEE) structures. Then the ICS-FEM formulations for free vibration calculation of FGMEE structures were deduced. In FGMEE structures, the true parameters at the Gaussian integration point were adopted directly to replace the homogenization in an element. The ICS-FEM provides a continuous system with a close-to-exact stiffness, which could be automatically and more easily generated for complicated domains, thus significantly decreasing the numerical error. To verify the accuracy and trustworthiness of ICS-FEM, we investigated several numerical examples and found that ICS-FEM simulated more accurately than the standard FEM. Also the effects of various equivalent stiffness matrices and the gradient function on the inherent frequency of FGMEE beams were studied.

1. Introduction

Functionally graded magnetoelastoelectric (FGMEE) materials are generally multiphase composites with continuously varying mechanical properties. FGMEE materials can convert magnetic, electric, and mechanical energy from one type into another and have received wide attention recently due to their electroelastic, magnetoelastic, and electromagnetic coupling effects [1, 2]. Therefore, FGMEE materials have been adopted in various smart structures, such as magnetic field probes, smart vibration sensors, optoelectronic devices, and medical ultrasonic transducers [3, 4]. The smart FGMEE structures are commonly fabricated in the beam pattern. However, to better apply FGMEE beams, researchers must analyse the statics and free vibration, and to predict the coupled response of FGMEE beams for practical applications, they should accurately calculate the properties of free vibrations.

Several computational techniques were proposed to investigate the electroelastic, magnetoelastic, and electromagnetic coupling effects of smart structures, such as finite element method (FEM), mesh-free method, and scaled

boundary FEM [5–10]. Bhangale and Ganesan analyzed the static behaviors of linear anisotropic FGMEE plates using semianalytical FEM and investigated the free vibration of FGMEE plates and cylindrical shells [11, 12]. A layerwise partial mixed FEM was proposed to model MEE plates [13]. Phoenix et al. analysed the static and dynamic behaviors of coupled MEE plates using FEM with the Reissner mixed variational theorem [14]. Buchanan used FEM to study the free vibrations of infinite magnetoelastoelectric cylinders [15]. However, these FEMs overestimated the stiffness of solid structures and were limited by low accuracy. Therefore, Sladek et al. proposed a mesh-free method to more accurately study the static behavior of a circular FGMEE plate [16], but this method reduced the computational effectiveness. Recently, Liu et al. solved the deformations of a nonuniform MEE plate using scaled boundary FEM [17]. By incorporating the nonlocal theory into scaled boundary FEM, Ke and Wang more accurately and effectively studied the free vibrations of MEE beams [18]. However, the effectiveness of scaled boundary FEM is still low and should be improved.

FEM, as a powerful computational tool to investigate MEE coupling behaviors, yet overestimates the stiffness of

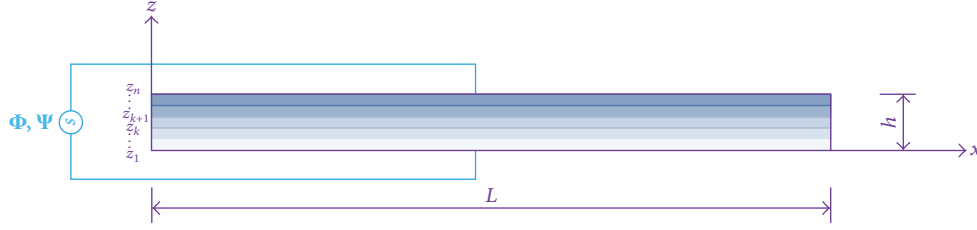


FIGURE 1: FGME beams: Cartesian coordinate system and geometric parameters.

FGME structures, which may result in locking behavior and inaccurate eigenvalue solutions [19]. To overcome these limitations, a series of cell-based smoothed FEM (CS-FEM) [20–26] and node-based, edge-based, or face-based smoothed FEMs [27–32] were proposed. In recent years, many CS-FEM-based formulations were proposed. Moreover, CS-FEM does not require the shape function derivatives or high generosity of program and is insensitive to mesh distortion because of the absence of isoparametric mapping.

CS-FEM has been successfully extended into dynamical control of piezoelectric sensors and actuators, topological optimization of linear piezoelectric micromotor, and analysis of static behaviors, frequency, and defects of piezoelectric structures [33–43]. Due to its versatility, CS-FEM becomes a simple and effective numerical tool to solve numerous electric and mechanical physical problems. However, the application of CS-FEM to investigate MEE properties is still a challenge.

In this work, free vibrations of FGME structures were studied. Inhomogeneous CS-FEM (ICS-FEM) for FGME materials was formulated by incorporating gradient smoothing into the standard FEM for the multi-physics field of FGME. Then the equations of free vibration computation were deduced under the multi-physics coupling field for FGME materials. Finally, FGME beams in the functional gradient exponential form or power law form were calculated under different boundary conditions. ICS-FEM outperformed FEM when compared with the reference solution.

This paper is organized as follows: Section 2 introduces the basic formulations for FGME materials. Section 3 briefly describes the properties of the FGME materials. Section 4 contains the detailed formulation of ICS-FEM. In Section 5, two numerical examples and the model of typical MEMS-based FGME energy harvester are investigated in detail. Final conclusions from the numerical results are drawn in Section 6.

2. Basic Formulations

The material properties of a functionally graded material (FGM) plate vary continuously, which is an advantage over the discontinuity across adjoining layers in a laminated plate. The wide range of engineering applications of FGM has attracted many scientists to investigate the behaviors of FGM.

Considering the transverse isotropy of the FGME medium [9, 44] and for the plane stress problem, we set

stress components $\sigma_y = \sigma_{yz} = \tau_{xy} = 0$, electric displacement component $D_y = 0$, and magnetic induction component $B_y = 0$. The geometric parameters and the chosen Cartesian coordinate system (x, y, z) are illustrated in Figure 1.

The basic formulations for MEE materials include equilibrium equations, geometric equations, and constitutive equations. The equilibrium equations are

$$\begin{aligned} \frac{\partial \sigma_x}{\partial x} + \frac{\partial \tau_{xz}}{\partial z} &= 0, \\ \frac{\partial \tau_{xz}}{\partial x} + \frac{\partial \sigma_z}{\partial z} &= 0, \\ \frac{\partial D_x}{\partial x} + \frac{\partial D_z}{\partial z} &= 0, \\ \frac{\partial B_x}{\partial x} + \frac{\partial B_z}{\partial z} &= 0, \end{aligned} \quad (1)$$

where σ_x , σ_z , and τ_{xz} denote stress components; D_x and D_z are electric displacement components; B_x and B_z are magnetic induction components.

The geometric equations are

$$\begin{aligned} S_x &= \frac{\partial u}{\partial x}, \\ S_z &= \frac{\partial w}{\partial z}, \\ S_{xz} &= \frac{\partial w}{\partial x} + \frac{\partial u}{\partial z}, \\ E_x &= -\frac{\partial \Phi}{\partial x}, \\ E_z &= -\frac{\partial \Phi}{\partial z}, \\ H_x &= -\frac{\partial \Psi}{\partial x}, \\ H_z &= -\frac{\partial \Psi}{\partial z}, \end{aligned} \quad (2)$$

where S_x , S_z , and S_{xz} denote strain components; u and w are displacement components; E_x and E_z are electric field components; Φ is electrical potential; H_x and H_z are magnetic field components; Ψ is magnetic potential.

The constitutive equations are

$$\begin{aligned}
\begin{Bmatrix} \sigma_x \\ \sigma_z \\ \tau_{xz} \end{Bmatrix} &= \begin{bmatrix} C_{11} & C_{13} & 0 \\ C_{13} & C_{33} & 0 \\ 0 & 0 & C_{44} \end{bmatrix} \begin{Bmatrix} S_x \\ S_z \\ S_{xz} \end{Bmatrix} + \begin{bmatrix} 0 & e_{31} \\ 0 & e_{33} \\ e_{15} & 0 \end{bmatrix} \begin{Bmatrix} E_x \\ E_z \end{Bmatrix} \\
&+ \begin{bmatrix} 0 & q_{31} \\ 0 & q_{33} \\ q_{15} & 0 \end{bmatrix} \begin{Bmatrix} H_x \\ H_z \end{Bmatrix}, \\
\begin{Bmatrix} D_x \\ D_z \end{Bmatrix} &= \begin{bmatrix} 0 & 0 & e_{15} \\ e_{31} & e_{33} & 0 \end{bmatrix} \begin{Bmatrix} S_x \\ S_z \\ S_{xz} \end{Bmatrix} + \begin{bmatrix} \epsilon_{11} & 0 \\ 0 & \epsilon_{33} \end{bmatrix} \begin{Bmatrix} E_x \\ E_z \end{Bmatrix} \\
&+ \begin{bmatrix} m_{11} & 0 \\ 0 & m_{33} \end{bmatrix} \begin{Bmatrix} H_x \\ H_z \end{Bmatrix}, \\
\begin{Bmatrix} B_x \\ B_z \end{Bmatrix} &= \begin{bmatrix} 0 & 0 & q_{15} \\ q_{31} & q_{33} & 0 \end{bmatrix} \begin{Bmatrix} S_x \\ S_z \\ S_{xz} \end{Bmatrix} + \begin{bmatrix} m_{11} & 0 \\ 0 & m_{33} \end{bmatrix} \begin{Bmatrix} E_x \\ E_z \end{Bmatrix} \\
&+ \begin{bmatrix} \mu_{11} & 0 \\ 0 & \mu_{33} \end{bmatrix} \begin{Bmatrix} H_x \\ H_z \end{Bmatrix},
\end{aligned} \tag{3}$$

where C_{ij} , ϵ_{ij} , and μ_{ij} are the elastic, dielectric, and magnetic permeability coefficients, respectively; e_{ij} , q_{ij} , and m_{ij} are piezo-electric, piezomagnetic, and magnetoelectric coefficients, respectively. For FGMEE materials, we have

$$\begin{aligned}
C_{ij} &= C_{ij}^0 f(z), \\
\epsilon_{ij} &= \epsilon_{ij}^0 f(z), \\
\mu_{ij} &= \mu_{ij}^0 f(z), \\
e_{ij} &= e_{ij}^0 f(z), \\
q_{ij} &= q_{ij}^0 f(z), \\
m_{ij} &= m_{ij}^0 f(z),
\end{aligned} \tag{4}$$

where $f(z)$ is an arbitrary function; C_{ij}^0 and $\epsilon_{ij}^0, \mu_{ij}^0, e_{ij}^0, q_{ij}^0$, and m_{ij}^0 are the values on the plane $z = 0$.

3. FGMEE Materials

An FGMEE structure is characterized by the high heterogeneity of material properties with a distribution prescribing the volume fractions of constituent phases. For particular analysis, it is functional to idealize them as continua with smooth gradual variation of material properties in the spatial coordinates. Hence, the proper micromechanical model should be able to characterize the material property distribution of a system in accurate sense.

Previous literatures focus on two types of gradation methods widely applied to solve many problems. Among

various methods for composites, some are also used for FGMEE materials, including the exponential and Voigt rule of mixture scheme.

For FGMEE materials with exponential variation in the thickness direction (z -direction), (4) can be rewritten as

$$\begin{aligned}
C_{ij} &= C_{ij}^0 e^{\eta z/h}, \\
\epsilon_{ij} &= \epsilon_{ij}^0 e^{\eta z/h}, \\
\mu_{ij} &= \mu_{ij}^0 e^{\eta z/h}, \\
e_{ij} &= e_{ij}^0 e^{\eta z/h}, \\
q_{ij} &= q_{ij}^0 e^{\eta z/h}, \\
m_{ij} &= m_{ij}^0 e^{\eta z/h},
\end{aligned} \tag{5}$$

where η is the exponential factor governing the degree of z -direction gradient, h is the thickness, the superscript 0 indicates the z -independent coefficients, and $\eta = 0$ in homogeneous MEE materials.

The volume fraction of an FGMEE structure across the thickness direction is assumed as a simple power law type as follows:

$$V_B = \left(\frac{2z + h}{2h} \right)^n, \tag{6}$$

where $-h/2 \leq z \leq h/2$ and n is the power law index. The bottom surface of the material ($z = -h/2$) is V_C whereas the top surface ($z = h/2$) is V_B . The total volume of the constituents should be

$$V_C + V_B = 1. \tag{7}$$

Based on (6) and (7), the effective material property is defined as follows:

$$(\text{MC})_{\text{eff}} = (\text{MC})_{\text{top}} V_B + (\text{MC})_{\text{bottom}} V_C, \tag{8}$$

where "MC" is general notation for material property. With (3), the effective coefficients can be written as

$$\begin{aligned}
C_{\text{eff}} &= (C_B - C_C) V_B + C_C, \\
\epsilon_{\text{eff}} &= (\epsilon_B - \epsilon_C) V_B + \epsilon_C, \\
\mu_{\text{eff}} &= (\mu_B - \mu_C) V_B + \mu_C, \\
e_{\text{eff}} &= (e_B - e_C) V_B + e_C, \\
q_{\text{eff}} &= (q_B - q_C) V_B + q_C, \\
m_{\text{eff}} &= (m_B - m_C) V_B + m_C,
\end{aligned} \tag{9}$$

where "eff" stands for effective properties corresponding to a specific value of n . Material coefficients of piezoelectric BaTiO₃, magnetostrictive CoFe₂O₄, and MEE BaTiO₃-CoFe₂O₄ are given in Table 1. Figure 2 depicts the through-the-thickness distribution of the volume fraction changing with different values of n . For $n = 1.0$, the variation of effective material property is linear.

TABLE 1: Magneto-electroelastic coefficients of material properties [6].

Material constants	CoFe ₂ O ₄	BaTiO ₃ -CoFe ₂ O ₄	BaTiO ₃
C_{11} 10 ⁹ N/m ²	286	200	166
C_{12} 10 ⁹ N/m ²	173	110	77
C_{13} 10 ⁹ N/m ²	170	110	78
C_{33} 10 ⁹ N/m ²	269.5	190	162
C_{44} 10 ⁹ N/m ²	45.3	45	43
e_{31} C/m ²	0	-3.5	-4.4
e_{33} C/m ²	0	11	18.6
e_{15} C/m ²	0	0	11.6
ϵ_{11} 10 ⁻⁹ C/Vm	0.08	0.9	11.2
ϵ_{33} 10 ⁻⁹ C/Vm	0.093	7.5	12.6
μ_{11} 10 ⁻⁴ Ns ² /C ²	-5.9	-1.5	0.05
μ_{33} 10 ⁻⁴ Ns ² /C ²	1.57	0.75	0.1
q_{31} N/Am	580	200	0
q_{33} N/Am	700	260	0
q_{15} N/Am	560	180	0
m_{11} 10 ⁻¹² Ns/VC	0	6.0	0
m_{33} 10 ⁻¹² Ns/VC	0	2500	0
ρ kgm ⁻³	5730	5730	5730

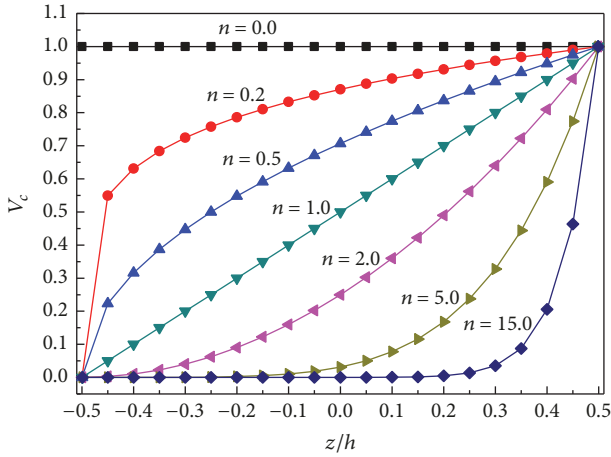


FIGURE 2: Variation of the volume fraction function versus the non-dimensional thickness z/h with varying n .

4. ICS-FEM

The solution domain Ω is discretized into n_p elements containing N_n nodes, the approximation displacement $\bar{\mathbf{u}}$, the approximation electrical potential $\bar{\Phi}$, and the approximation magnetic potential $\bar{\Psi}$. For FGME materials, we have

$$\bar{\mathbf{u}} = \sum_{i=1}^{n_p} N_i^u u_i = \mathbf{N}_u \mathbf{u},$$

$$\bar{\Phi} = \sum_{i=1}^{n_p} N_i^\Phi \Phi_i = \mathbf{N}_\Phi \Phi,$$

$$\bar{\Psi} = \sum_{i=1}^{n_p} N_i^\Psi \Psi_i = \mathbf{N}_\Psi \Psi, \quad (10)$$

where \mathbf{u} , Φ , and Ψ are the vectors of node displacement, node electrical potential, and node magnetic potential, respectively; \mathbf{N}_u , \mathbf{N}_Φ , and \mathbf{N}_Ψ are displacement shape, electrical potential shape, and magnetic potential shape functions of ICS-FEM, respectively. \mathbf{N}_u , \mathbf{N}_Φ , and \mathbf{N}_Ψ were expressed in similar shape functions. Four-node element divided into four smoothing subdomains [27], field nodes, edge smoothing nodes, center smoothing nodes, edge Gaussian point, outer normal vector distribution, and shape function values are shown in Figure 3.

At any point \mathbf{x}^k in the smoothing subdomain Ω_i^k , the smoothed strain $\bar{\mathbf{S}}(\mathbf{x}^k)$, smoothed electric field $\bar{\mathbf{E}}(\mathbf{x}^k)$, and smoothed magnetic field $\bar{\mathbf{H}}(\mathbf{x}^k)$ are

$$\bar{\mathbf{S}}(\mathbf{x}^k) = \int_{\Omega_i^k} \mathbf{S}(\mathbf{x}) \kappa(\mathbf{x} - \mathbf{x}^k) d\Omega,$$

$$\bar{\mathbf{E}}(\mathbf{x}^k) = \int_{\Omega_i^k} \mathbf{E}(\mathbf{x}) \kappa(\mathbf{x} - \mathbf{x}^k) d\Omega, \quad (11)$$

$$\bar{\mathbf{H}}(\mathbf{x}^k) = \int_{\Omega_i^k} \mathbf{H}(\mathbf{x}) \kappa(\mathbf{x} - \mathbf{x}^k) d\Omega,$$

where $\mathbf{S}(\mathbf{x})$, $\mathbf{E}(\mathbf{x})$, and $\mathbf{H}(\mathbf{x})$ are the strain, electric field, and magnetic field in FEM, respectively; $\kappa(\mathbf{x} - \mathbf{x}^k)$ is the constant function:

$$\kappa(\mathbf{x} - \mathbf{x}^k) = \begin{cases} \frac{1}{A_i^k} & \mathbf{x} \in \Omega_i^k \\ 0 & \mathbf{x} \notin \Omega_i^k, \end{cases} \quad (12)$$

where

$$A_i^k = \int_{\Omega_i^k} d\Omega. \quad (13)$$

Substituting (12) into (11), we get

$$\bar{\mathbf{S}}(\mathbf{x}^k) = \frac{1}{A_i^k} \int_{\Gamma_i^k} \mathbf{n}_u^k \mathbf{u} d\Gamma,$$

$$\bar{\mathbf{E}}(\mathbf{x}^k) = \frac{1}{A_i^k} \int_{\Gamma_i^k} \mathbf{n}_\Phi^k \Phi d\Gamma, \quad (14)$$

$$\bar{\mathbf{H}}(\mathbf{x}^k) = \frac{1}{A_i^k} \int_{\Gamma_i^k} \mathbf{n}_\Psi^k \Psi d\Gamma,$$

where Γ_i^k is the boundary of Ω_i^k ; \mathbf{n}_u^k , \mathbf{n}_Φ^k , and \mathbf{n}_Ψ^k are the outer normal vector matrices of the boundary:

$$\mathbf{n}_u^k = \begin{bmatrix} n_x^k & 0 \\ 0 & n_z^k \\ n_z^k & n_x^k \end{bmatrix},$$

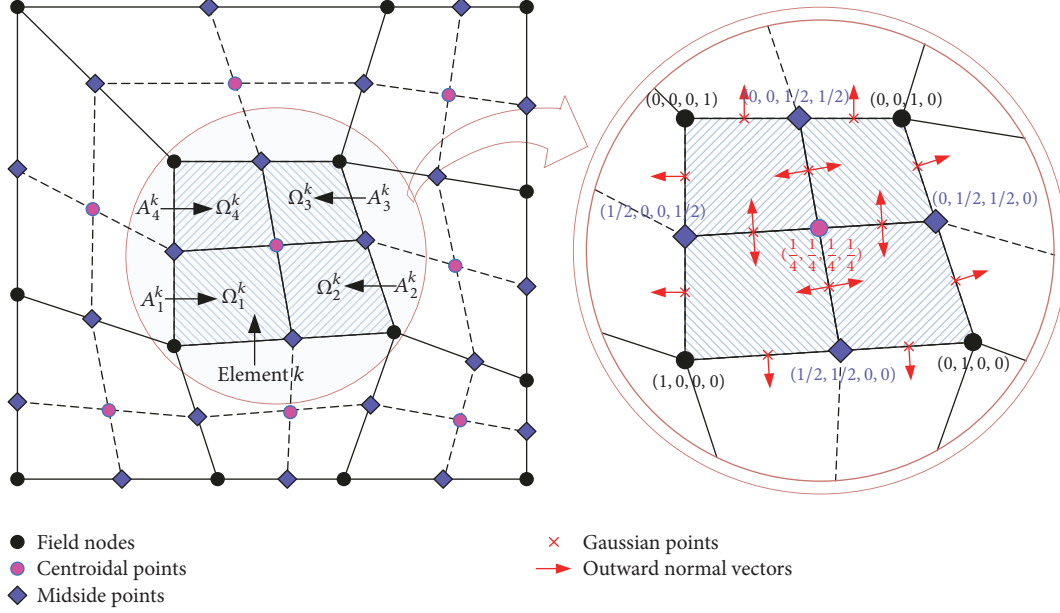


FIGURE 3: Smoothing subdomains and the values of shape functions.

$$\mathbf{n}_\Phi^k = \begin{bmatrix} n_x^k \\ n_z^k \end{bmatrix},$$

$$\mathbf{n}_\Psi^k = \begin{bmatrix} n_x^k \\ n_z^k \end{bmatrix}.$$

(15)

Eqs. (14) can be rewritten as

$$\bar{\mathbf{S}}(\mathbf{x}^k) = \sum_{i=1}^{n_e} \bar{\mathbf{B}}_u^i(\mathbf{x}^k) \mathbf{u}_i,$$

$$\bar{\mathbf{E}}(\mathbf{x}^k) = -\sum_{i=1}^{n_e} \bar{\mathbf{B}}_\Phi^i(\mathbf{x}^k) \Phi_i,$$

$$\bar{\mathbf{H}}(\mathbf{x}^k) = -\sum_{i=1}^{n_e} \bar{\mathbf{B}}_\Psi^i(\mathbf{x}^k) \Psi_i,$$

(16)

where n_e is the number of smoothing elements

$$\bar{\mathbf{B}}_u^i(\mathbf{x}^k) = \frac{1}{A_i^k} \int_{\Gamma^k} \begin{bmatrix} N_i^u n_x^k & 0 \\ 0 & N_i^u n_z^k \\ N_i^u n_z^k & N_i^u n_x^k \end{bmatrix} d\Gamma,$$

$$\bar{\mathbf{B}}_\Phi^i(\mathbf{x}^k) = \frac{1}{A_i^k} \int_{\Gamma^k} \begin{bmatrix} N_i^\Phi n_x^k \\ N_i^\Phi n_z^k \end{bmatrix} d\Gamma,$$

$$\bar{\mathbf{B}}_\Psi^i(\mathbf{x}^k) = \frac{1}{A_i^k} \int_{\Gamma^k} \begin{bmatrix} N_i^\Psi n_x^k \\ N_i^\Psi n_z^k \end{bmatrix} d\Gamma.$$

(17)

At the Gaussian point of the smoothing boundary \mathbf{x}_b^G , (17) are rewritten as

$$\bar{\mathbf{B}}_u^i(\mathbf{x}^k) = \frac{1}{A_i^k} \sum_{b=1}^{n_b} \begin{pmatrix} N_i^u(\mathbf{x}_b^G) n_x^k & 0 \\ 0 & N_i^u(\mathbf{x}_b^G) n_z^k \\ N_i^u(\mathbf{x}_b^G) n_z^k & N_i^u(\mathbf{x}_b^G) n_x^k \end{pmatrix} l_b^k,$$

$$\bar{\mathbf{B}}_\Phi^i(\mathbf{x}^k) = \frac{1}{A_i^k} \sum_{b=1}^{n_b} \begin{pmatrix} N_i^\Phi(\mathbf{x}_b^G) n_x^k \\ N_i^\Phi(\mathbf{x}_b^G) n_z^k \end{pmatrix} l_b^k,$$

(18)

$$\bar{\mathbf{B}}_\Psi^i(\mathbf{x}^k) = \frac{1}{A_i^k} \sum_{b=1}^{n_b} \begin{pmatrix} N_i^\Psi(\mathbf{x}_b^G) n_x^k \\ N_i^\Psi(\mathbf{x}_b^G) n_z^k \end{pmatrix} l_b^k,$$

where l_b^k is the length of the smoothing boundary; n_b is the total number of boundaries for each smoothing subdomain.

As for the essential difference, FEM has to derive the shape function matrix of the element, but ICS-FEM avoids this step and simply uses the shape function at \mathbf{x}_b^G , which reduces the requirement for continuity of the shape function and improves the accuracy and convergence by the use of gradient smoothing.

The thermodynamic potential of a 2D FGMEE problem is given as

$$G = G(\mathbf{S}, \mathbf{E}, \mathbf{H}), \quad (19)$$

where \mathbf{S} , \mathbf{E} , and \mathbf{H} are independent variables of strain, electric field, and magnetic field, respectively.

By applying (1) into (19), we get the variational expression of MEE plane:

$$G = \left(\frac{1}{2} \mathbf{S}^T \mathbf{C} \mathbf{S} \right) - \left(\frac{1}{2} \mathbf{E}^T \boldsymbol{\varepsilon} \mathbf{E} \right) - \left(\frac{1}{2} \mathbf{H}^T \boldsymbol{\mu} \mathbf{H} \right) - \mathbf{S} \mathbf{e} \mathbf{E} \\ - \mathbf{S} \mathbf{q} \mathbf{H} - \mathbf{E} \mathbf{m} \mathbf{H}.$$

(20)

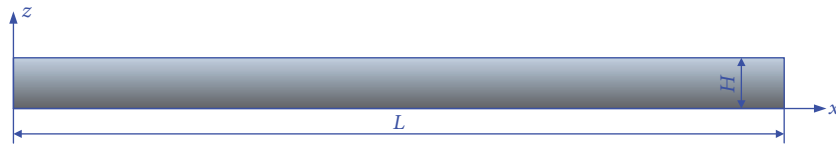
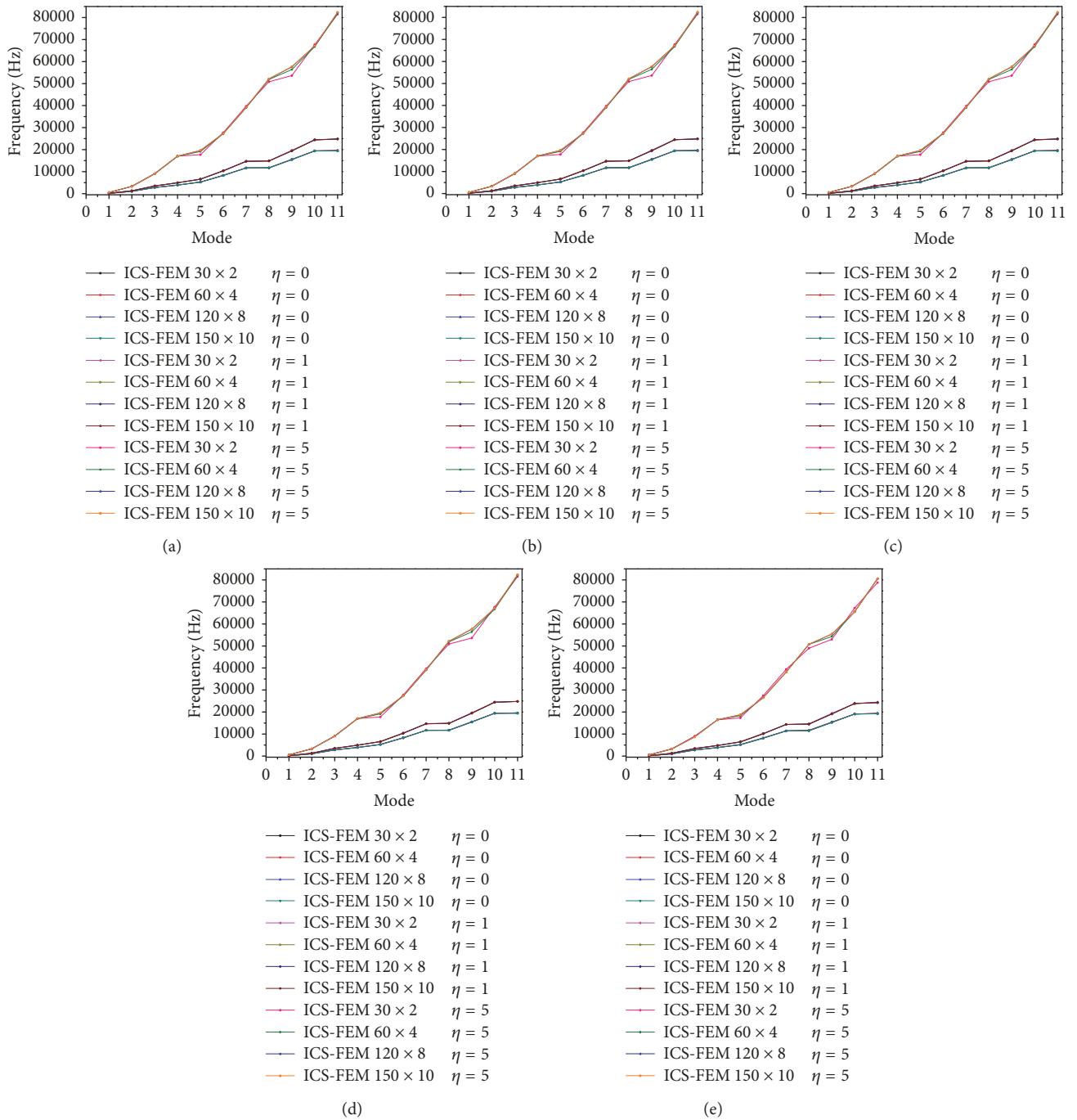


FIGURE 4: Geometry of an FGME beam and the coordinates.

FIGURE 5: Structural frequencies (a) f_{uu} ; (b) f_{eq} ; (c) f_{eq-re} ; (d) $f_{eq-\Phi\Phi}$; (e) $f_{eq-\Psi\Psi}$ of clamp-free $BaTiO_3-CoFe_2O_4$ FGME beams.

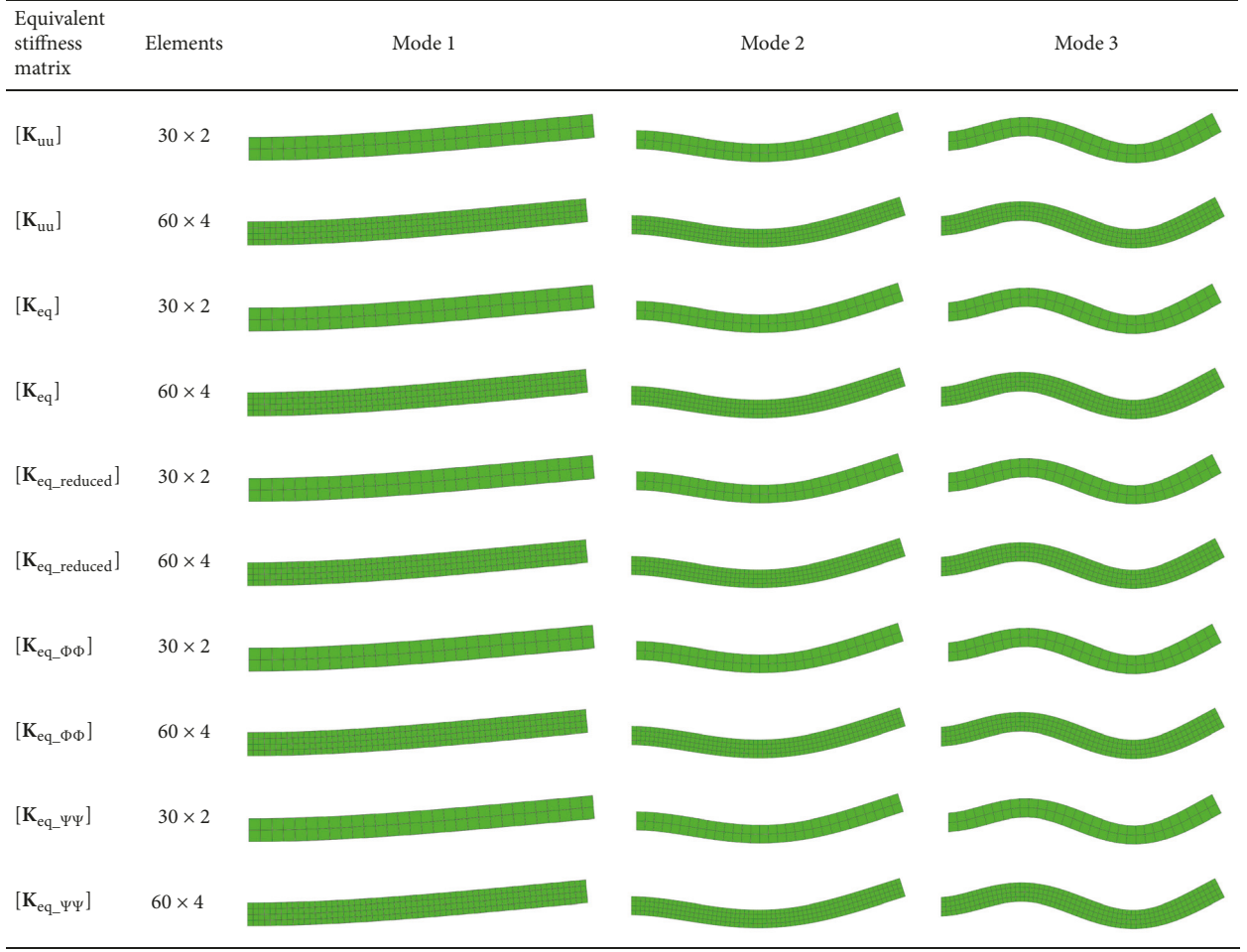


FIGURE 6: The first- to third-order modes of clamp-free BaTiO₃-CoFe₂O₄ FGME beams using different elements with exponential factor $\eta = 1.0$ by ICS-FEM.

By minimizing (20) for nodal variables of shape functions for strain-displacement, electric field–electric potential, and magnetic field–magnetic potential, we get the ICS-FEM equations for MEE plane:

$$\begin{aligned}
 & [[\mathbf{K}_{uu}] - \omega^2 [\mathbf{M}]] \{\mathbf{u}\} + [\mathbf{K}_{u\Phi}] \{\Phi\} + [\mathbf{K}_{u\Psi}] \{\Psi\} = 0, \\
 & [\mathbf{K}_{u\Phi}]^T \{\mathbf{u}\} - [\mathbf{K}_{\Phi\Phi}] \{\Phi\} - [\mathbf{K}_{\Phi\Psi}] \{\Psi\} = 0, \\
 & [\mathbf{K}_{u\Psi}]^T \{\mathbf{u}\} - [\mathbf{K}_{\Phi\Psi}]^T \{\Phi\} - [\mathbf{K}_{\Psi\Psi}] \{\Psi\} = 0,
 \end{aligned} \quad (21)$$

where ω is the eigenvalues.

Different elemental stiffness matrices used for FGME beams are expressed as follows:

$$\begin{aligned}
 \mathbf{K}_{uu} &= \sum_{i=1}^{n_c} \bar{\mathbf{B}}_u^{iT} [\mathbf{C}] \bar{\mathbf{B}}_u^i A_i^k, \\
 \mathbf{K}_{u\Phi} &= \sum_{i=1}^{n_c} \bar{\mathbf{B}}_u^{iT} [\mathbf{e}] \bar{\mathbf{B}}_\Phi^i A_i^k, \\
 \mathbf{K}_{u\Psi} &= - \sum_{k=1}^{n_c} \bar{\mathbf{B}}_u^{iT} [\mathbf{q}] \bar{\mathbf{B}}_\Psi^i A_i^k,
 \end{aligned}$$

$$\mathbf{K}_{\Phi\Psi} = \sum_{i=1}^{n_c} \bar{\mathbf{B}}_\Phi^{iT} [\mathbf{m}] \bar{\mathbf{B}}_\Psi^i A_i^k,$$

$$\mathbf{K}_{\Phi\Phi} = \sum_{i=1}^{n_c} \bar{\mathbf{B}}_\Phi^{iT} [\boldsymbol{\varepsilon}] \bar{\mathbf{B}}_\Phi^i A_i^k,$$

$$\mathbf{K}_{\Psi\Psi} = \sum_{i=1}^{n_c} \bar{\mathbf{B}}_\Psi^{iT} [\boldsymbol{\mu}] \bar{\mathbf{B}}_\Psi^i A_i^k,$$

$$\mathbf{M} = \sum_e \mathbf{M}^e,$$

$$\mathbf{M}^e = \text{diag} \{m_1, m_1, m_2, m_2, m_3, m_3, m_4, m_4\},$$

(22)

where $n_c = n_p \times n_e$; $m_i = \rho_i t A_i^k$ ($i = 1, 2, 3, 4$) is the mass of smoothing element i ; t is the smoothing element thickness; ρ_i is density of Gaussian integration point in smoothing subdomain i ; $[\mathbf{C}]$, $[\boldsymbol{\varepsilon}]$, $[\boldsymbol{\mu}]$, $[\mathbf{e}]$, $[\mathbf{q}]$, and $[\mathbf{m}]$ are the matrices of elastic constant, dielectric coefficient, magnetic permeability, piezomagnetic coefficient, piezomagnetic coefficient, and magnetolectric coefficient, respectively.

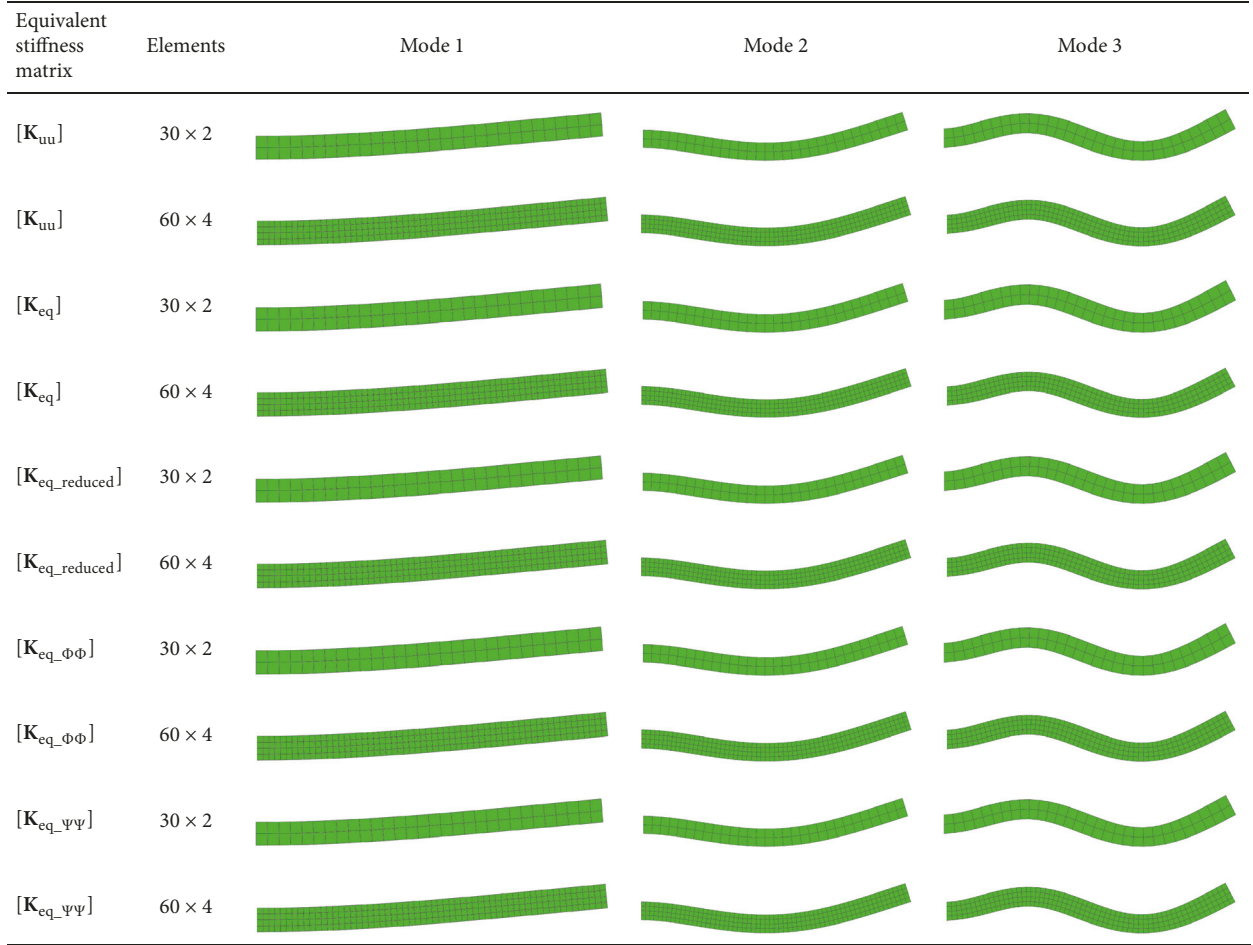


FIGURE 7: The first- to third-order modes of clamp-free $\text{BaTiO}_3\text{-CoFe}_2\text{O}_4$ FGME beams using different elements with exponential factor $\eta = 5.0$ by ICS-FEM.



FIGURE 8: Domain discretization using four-node extremely irregular elements.

The inhomogeneous smoothing element was adopted to calculate its stiffness matrix. Because the parameters of four smoothing subdomains A_i^k ($i = 1, 2, 3, 4$) differed in element s , the actual parameters at the Gaussian integration point were taken directly to simulate the changes of material property in each element.

By eliminating the terms of electric and magnetic potentials using a condensation technique, we get the equivalent stiffness matrix $[\mathbf{K}_{eq}]$:

$$[\mathbf{K}_{eq}] \{\mathbf{u}\} + [\mathbf{M}] \{\ddot{\mathbf{u}}\} = 0, \quad (23)$$

where

$$[\mathbf{K}_{eq}] = [\mathbf{K}_{uu}] + [\mathbf{K}_{u\Phi}] [\mathbf{K}_{II}]^{-1} [\mathbf{K}_I] \\ + [\mathbf{K}_{u\Psi}] [\mathbf{K}_{IV}]^{-1} [\mathbf{K}_{III}],$$

$$[\mathbf{K}_I] = [\mathbf{K}_{u\Phi}]^T - [\mathbf{K}_{\Phi\Psi}] [\mathbf{K}_{\Psi\Psi}]^{-1} [\mathbf{K}_{u\Psi}]^T, \\ [\mathbf{K}_{II}] = [\mathbf{K}_{\Phi\Phi}] - [\mathbf{K}_{\Phi\Psi}] [\mathbf{K}_{\Psi\Psi}]^{-1} [\mathbf{K}_{\Phi\Psi}]^T, \\ [\mathbf{K}_{III}] = [\mathbf{K}_{u\Psi}]^T - [\mathbf{K}_{\Phi\Psi}]^T [\mathbf{K}_{\Phi\Phi}]^{-1} [\mathbf{K}_{u\Phi}]^T, \\ [\mathbf{K}_{IV}] = [\mathbf{K}_{\Psi\Psi}] - [\mathbf{K}_{\Phi\Psi}]^T [\mathbf{K}_{\Phi\Phi}]^{-1} [\mathbf{K}_{\Phi\Psi}]. \quad (24)$$

The eigenvectors corresponding to Φ and Ψ are given as

$$\Phi = [\mathbf{K}_{II}]^{-1} [\mathbf{K}_I] \{\mathbf{u}\}, \quad (25) \\ \Psi = [\mathbf{K}_{IV}]^{-1} [\mathbf{K}_{III}] \{\mathbf{u}\}.$$

To study the effect of magnetolectric constant on system frequencies, we derived $[\mathbf{K}_{eq_reduced}]$ by neglecting the magnetolectric coupling effect.

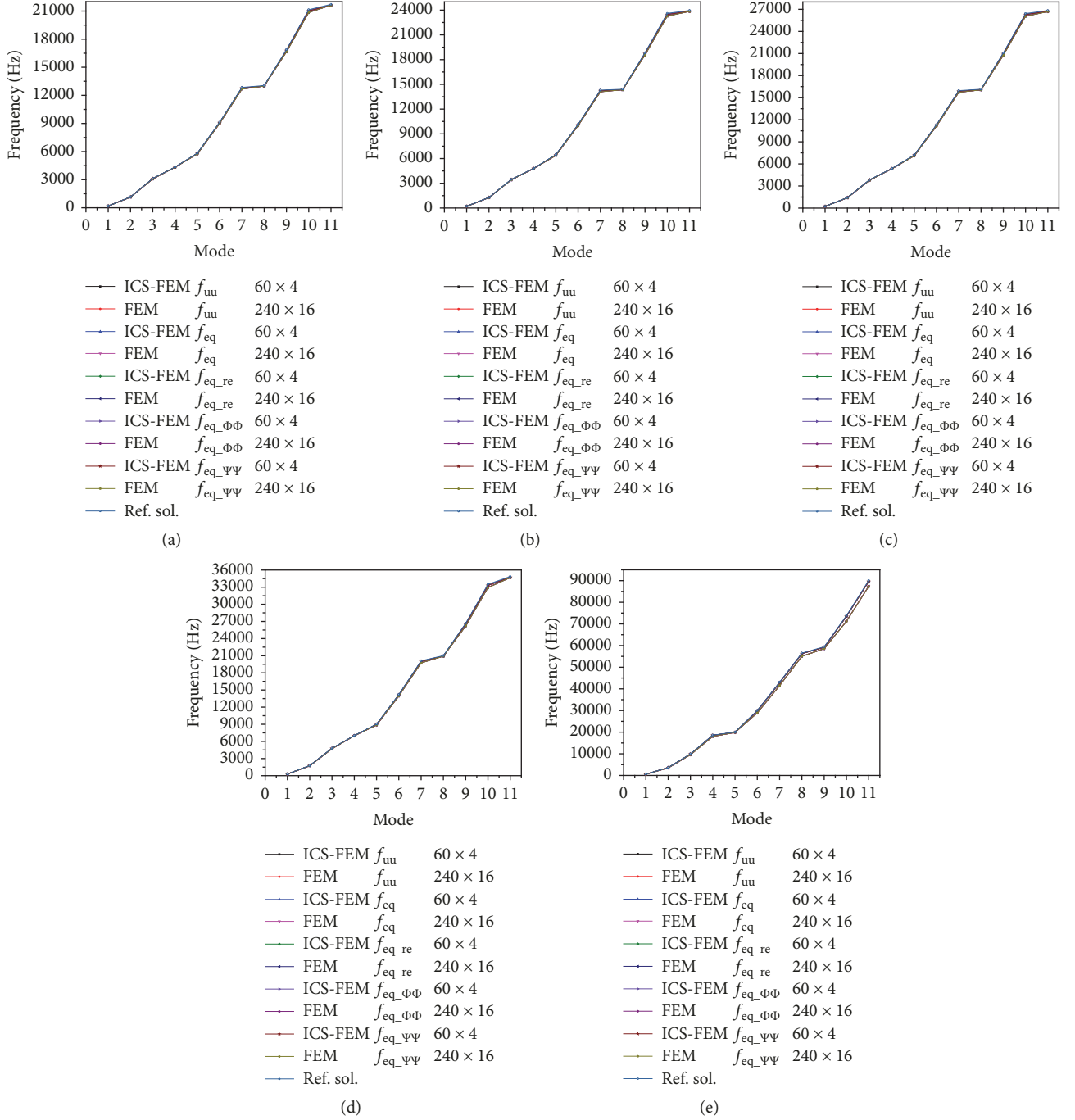


FIGURE 9: Structural frequencies f of clamp-free CoFe_2O_4 FGME beams with exponential factor $\eta =$ (a) 0, (b) 0.5, (c) 1.0, (d) 2.0, and (e) 5.0.

By making $[\mathbf{K}_{\Phi\Psi}] = 0$, we get the reduced cell-based finite element equations:

$$\begin{aligned}
 & [[\mathbf{K}_{uu}] - \omega^2 [\mathbf{M}]] \{\mathbf{u}\} + [\mathbf{K}_{u\Phi}] \{\Phi\} + [\mathbf{K}_{u\Psi}] \{\Psi\} = 0, \\
 & [\mathbf{K}_{u\Phi}]^T \{\mathbf{u}\} - [\mathbf{K}_{\Phi\Phi}] \{\Phi\} = 0, \quad (26) \\
 & [\mathbf{K}_{u\Psi}]^T \{\mathbf{u}\} - [\mathbf{K}_{\Psi\Psi}] \{\Psi\} = 0.
 \end{aligned}$$

The reduced stiffness matrix $[\mathbf{K}_{\text{eq_reduced}}]$ is

$$\begin{aligned}
 [\mathbf{K}_{\text{eq_reduced}}] &= [\mathbf{K}_{uu}] + [\mathbf{K}_{u\Phi}] [\mathbf{K}_{\Phi\Phi}]^{-1} [\mathbf{K}_{u\Phi}]^T \\
 &\quad + [\mathbf{K}_{u\Psi}] [\mathbf{K}_{\Psi\Psi}]^{-1} [\mathbf{K}_{u\Psi}]^T. \quad (27)
 \end{aligned}$$

To evaluate the effect of PE phase on beam frequency, we derived the stiffness matrix $[\mathbf{K}_{\text{eq_}\Phi\Phi}]$ by setting the magnetic potential = 0:

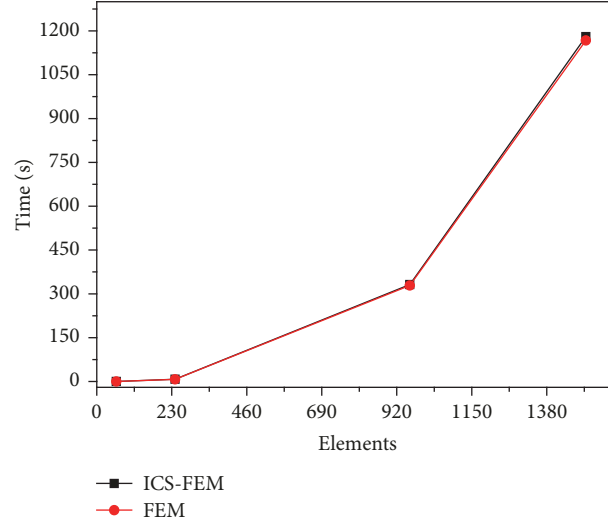


FIGURE 10: Comparison of computational efficiency.

TABLE 2: List of f used in the study.

Structural frequency	Matrix used to compute the structural frequency
f_{uu}	$[\mathbf{K}_{uu}]$
f_{eq}	$[\mathbf{K}_{eq}]$
$f_{eq, re}$	$[\mathbf{K}_{eq, reduced}]$
$f_{eq, \Phi\Phi}$	$[\mathbf{K}_{eq, \Phi\Phi}]$
$f_{eq, \Psi\Psi}$	$[\mathbf{K}_{eq, \Psi\Psi}]$

$$[\mathbf{K}_{eq, \Phi\Phi}] = [\mathbf{K}_{uu}] + [\mathbf{K}_{u\Phi}] [\mathbf{K}_{\Phi\Phi}]^{-1} [\mathbf{K}_{u\Phi}]^T. \quad (28)$$

To study the magnetic effect of PM phase on system frequency, we obtained $[\mathbf{K}_{eq, \Psi\Psi}]$ by plugging electric potential to zero in (26):

$$[\mathbf{K}_{eq, \Psi\Psi}] = [\mathbf{K}_{uu}] + [\mathbf{K}_{u\Psi}] [\mathbf{K}_{\Psi\Psi}]^{-1} [\mathbf{K}_{u\Psi}]^T. \quad (29)$$

5. Results and Discussion

5.1. C-F Beam. The free vibrations on FGME beams were calculated by changing the exponential factor (Figure 4). The material properties of FGME beams were governed by the z -direction exponential variation. The following geometrical parameters were considered: length $L = 0.3$ m and width $H = 0.02$ m with the assumption of plane stress. Boundary conditions were $u = w = \Phi = \Psi = 0$ at the clamped end. Table 2 gives the various structural frequencies in the study.

Firstly, the convergence of ICS-FEM was verified by using $\text{BaTiO}_3\text{-CoFe}_2\text{O}_4$ FGME beams, with properties listed in Table 1. The natural frequencies of these beams were calculated using ICS-FEM with different meshes (30×2 , 60×4 , 120×8 , 150×10) (Figure 5). The simulation results with different meshes agree well, which prove the good convergence of ICS-FEM. The first- to third-order modes of clamp-free $\text{BaTiO}_3\text{-CoFe}_2\text{O}_4$ FGME beams using different elements

with exponential factor $\eta = 1.0$ and 5.0 were calculated by ICS-FEM, and the results were summarized in Figures 6 and 7, respectively. It was found that the first- to third-order modes of $\text{BaTiO}_3\text{-CoFe}_2\text{O}_4$ FGME beams in the same gradient distribution were basically not affected by equivalent stiffness matrix or mesh number. The first- to third-order modes of $\text{BaTiO}_3\text{-CoFe}_2\text{O}_4$ FGME beams were basically not different between $\eta = 1.0$ and 5.0 .

Secondly, the free vibration frequencies of CoFe_2O_4 FGME beams were studied by both ICS-FEM and FEM using extremely irregular elements, with domain discretization shown in Figure 8. The frequencies of clamp-free CoFe_2O_4 FGME beams with different values of exponential factor are shown in Figure 9; the first eleven natural frequencies calculated by ICS-FEM are smaller than those calculated by FEM. The validity of ICS-FEM is verified by the agreements between the calculations and the reference solutions. The shape of quadrilateral element in FEM cannot be severely distorted but was eliminated in ICS-FEM. ICS-FEM abstains from calculating the derivative of the shape functions of an element, and the area integral of the solution domain is converted to the boundary integral. The stiffness of FGME structures is improved because ICS-FEM does not require continuity of the shape function. The ICS-FEM provides a continuous system with a close-to-exact stiffness, which could be automatically and more easily generated for complicated domains, thus significantly decreasing the numerical error. The free vibration of CoFe_2O_4 FGME beam, a pure CoFe_2O_4 material without piezoelectric or magnetoelectric material coefficients, influences structural frequency f_{eq} because the magnetic effect is marginally higher compared with f_{uu} . $f_{\Phi\Phi}$ coincides with f_{uu} since piezoelectric phase is absent in CoFe_2O_4 . Similarly, $f_{eq, re}$ coincides with f_{eq} of the CoFe_2O_4 FGME beam as the magnetoelectric effect is absent in pure CoFe_2O_4 FGME beam. The natural frequencies of CoFe_2O_4 FGME beams increase with the rise of the exponential factor.

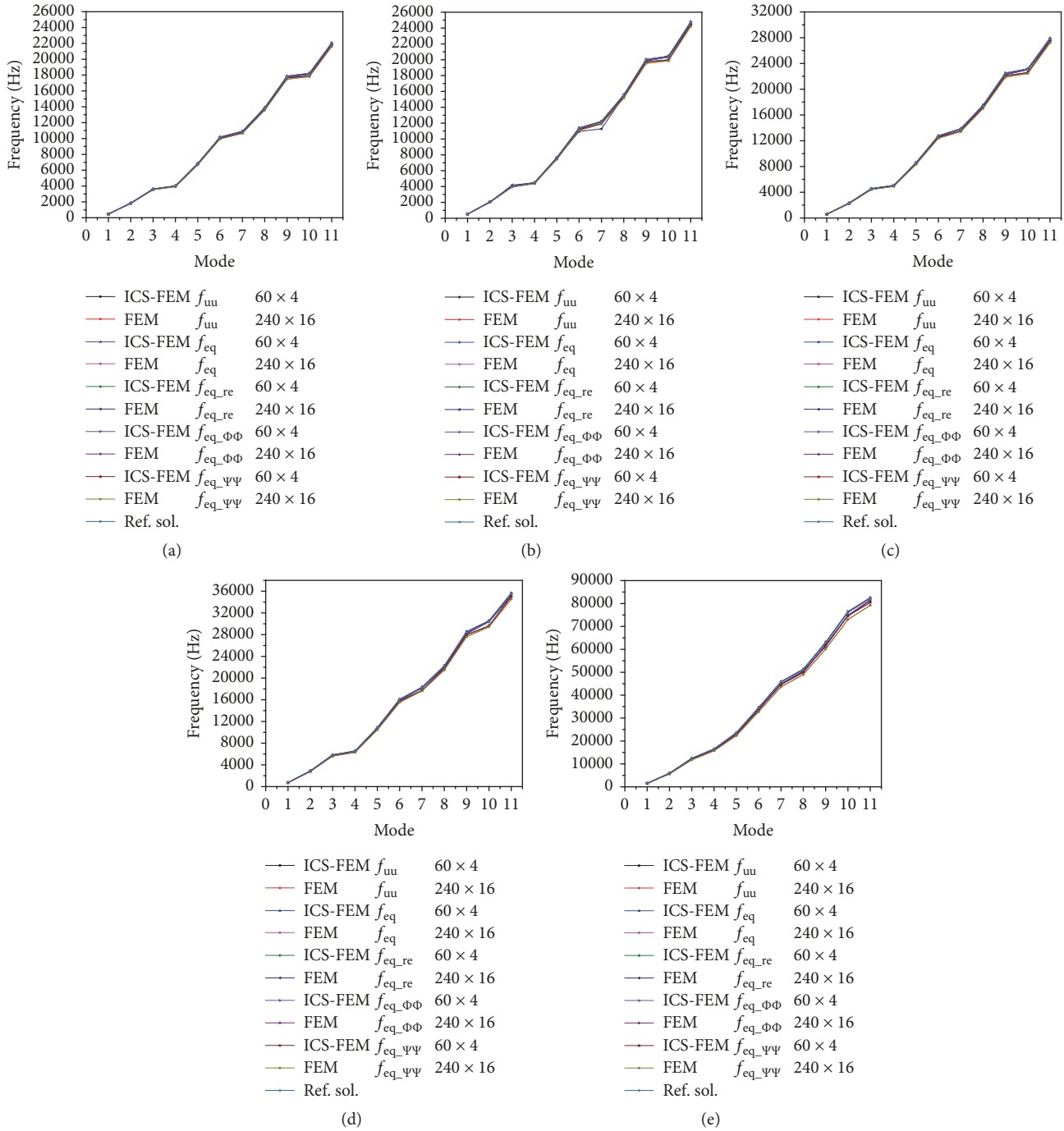


FIGURE 11: Structural frequencies f for simply supported $\text{BaTiO}_3\text{-CoFe}_2\text{O}_4$ FGME beams with exponential factor $\eta =$ (a) 0, (b) 0.5, (c) 1.0, (d) 2.0, and (e) 5.0.

Finally, the comparison of calculation time between ICS-FEM and FEM at Intel (R) Xeon (R) CPU E3-1220 v3 @ 3.10 GHz, 16 G RAM is shown in Figure 10, with the element number of 60, 240, 960, and 1500. As showed in Figure 10, the time required to solve algebraic equations by ICS-FEM is similar to that of FEM. Because the stiffness construction of ICS-FEM is based on smoothing cells inside each element, no coupling occurs between nodal degrees-of-freedom that are the distance of up to two elements. In other words, the

bandwidth of ICS-FEM stiffness matrix is the same as that of FEM. Nevertheless, ICS-FEM is more effective in terms of generalized displacement (including displacement, electrical potential and magnetic potential) and computational efficiency (computation time for the same accuracy).

5.2. *S-S Beam*. The free vibrations on $\text{BaTiO}_3\text{-CoFe}_2\text{O}_4$ FGME beams were studied by changing the gradient function form in Figure 4. The geometrical parameters were

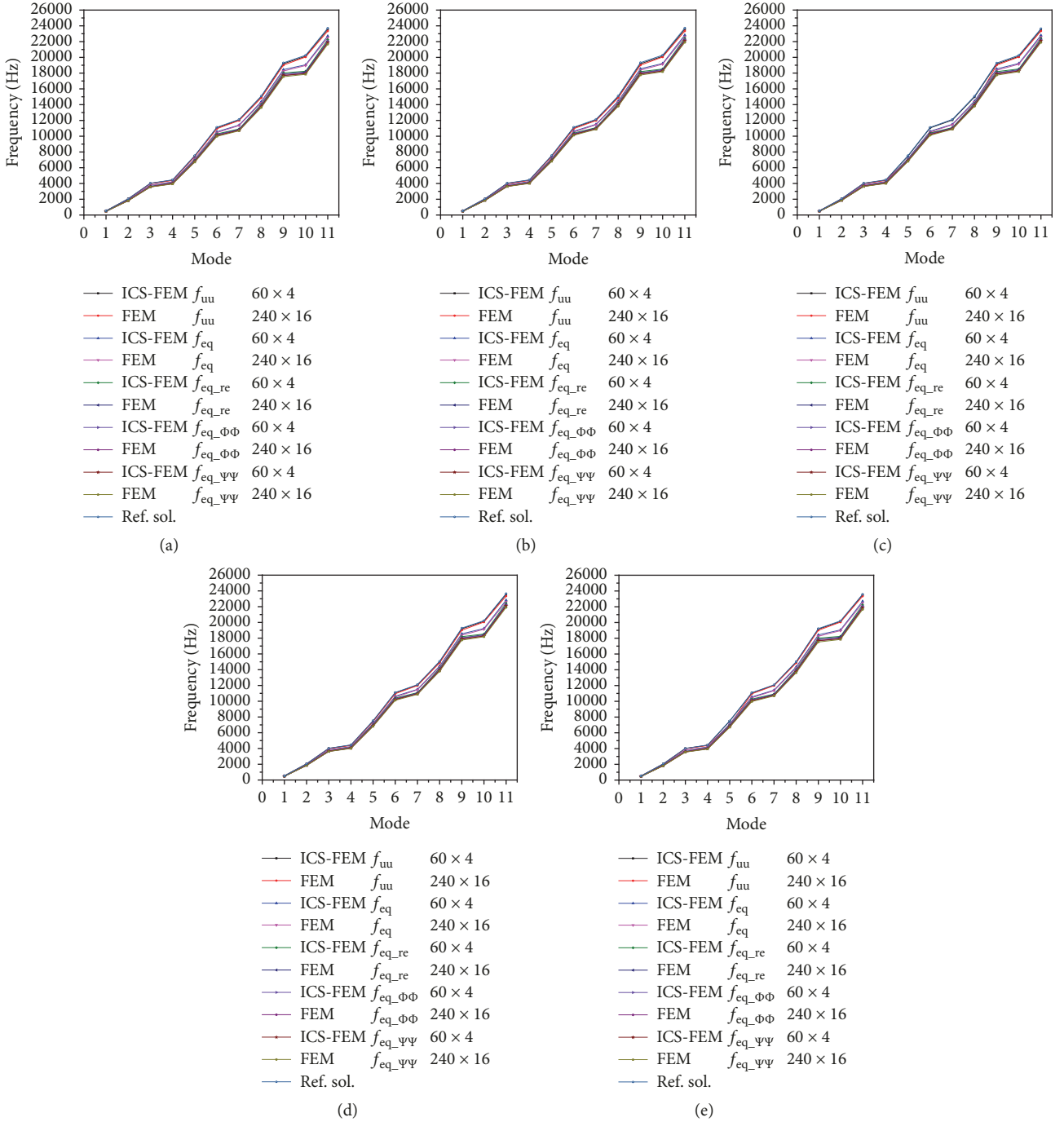


FIGURE 12: Structural frequencies f of simply supported $\text{BaTiO}_3\text{-CoFe}_2\text{O}_4$ FGME beams with power law index $n =$ (a) 0, (b) 1.0, (c) 5.0, (d) 10.0, and (e) 20.0.

the same as the C-F beam. The simply supported boundary conditions were used: $u = w = \Psi = \Phi = 0$ at $(x = 0, z = h/2)$ and $w = \Psi = \Phi = 0$ at $(x = L, z = h/2)$.

Firstly, the free vibration frequencies for $\text{BaTiO}_3\text{-CoFe}_2\text{O}_4$ FGME beams were calculated by both ICS-FEM with 60×4 meshes and FEM with 240×16 meshes (Figure 11). Results show the first eleven natural frequencies calculated by ICS-FEM are closer to the reference solutions than those calculated by FEM, indicating ICS-FEM is more efficient than

FEM due to the reduced number of meshes. The differences in natural frequencies f_{eq} , f_{eq_re} , and f_{eq_PhiPhi} are marginal, so the magnetic effect only slightly impacts the natural frequencies of FGME beams. The natural frequencies increase with the rise of the exponential factor.

Secondly, as for $\text{BaTiO}_3\text{-CoFe}_2\text{O}_4$ FGME beams with power law type ($n = 0, 1.0, 5.0, 10.0, 20.0$), the bottom surface ($z = -h/2$) is $\text{BaTiO}_3\text{-CoFe}_2\text{O}_4$ whereas the top surface ($z = h/2$) is CoFe_2O_4 . The free vibration frequencies for

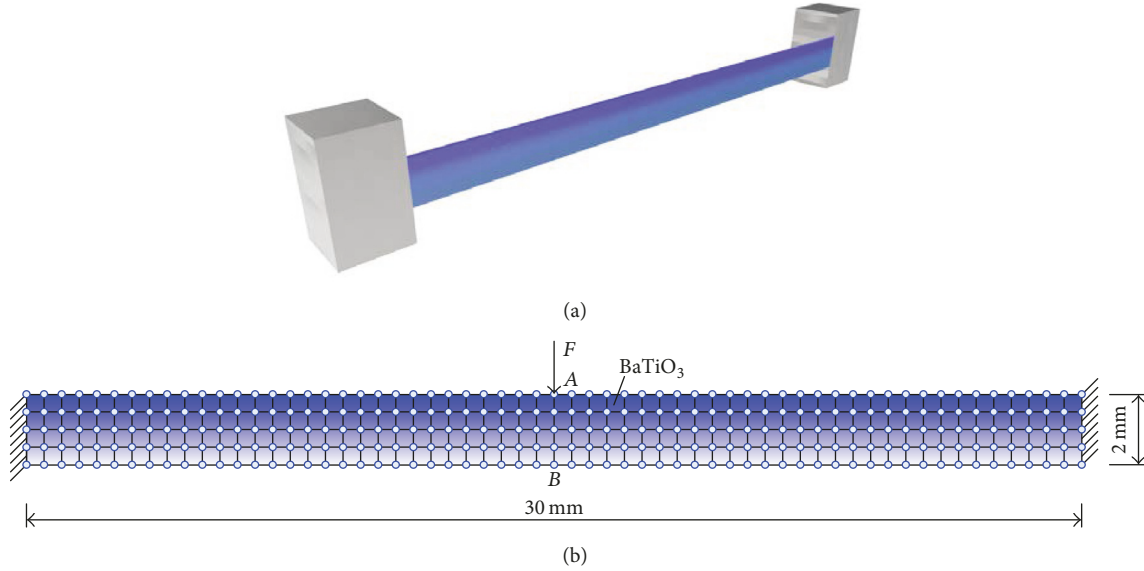


FIGURE 13: Typical MEMS-based energy harvester fabricated with BaTiO_3 FGME. (a) Model of the energy harvester; (b) simplified model of ICS-FEM.

FGMEE beams calculated by ICS-FEM with 60×4 meshes and FEM with 240×16 meshes are shown in Figure 12. Results show the first eleven natural frequencies calculated by ICS-FEM are closer to the reference solutions than those calculated by FEM. Also the differences in f_{eq} , $f_{\text{eq-re}}$, and $f_{\text{eq-}\Phi\Phi}$ are marginal, so the magnetic effect does not largely impact the natural frequencies of FGMEE beams. Meanwhile, the natural frequency of $\text{BaTiO}_3\text{-CoFe}_2\text{O}_4$ FGMEE beams is between those of $\text{BaTiO}_3\text{-CoFe}_2\text{O}_4$ MEE beams and CoFe_2O_4 MEE beams.

5.3. Typical MEMS-Based FGMEE Energy Harvester. The model of FGMEE energy harvester developed by ICS-FEM is shown in Figure 13. The free vibrations on the FGMEE energy harvester were studied by changing the exponential factor. The geometrical parameters were $L = 30$ mm, $H = 2$ mm, and its structure was fabricated with BaTiO_3 FGMEE.

The free vibration frequencies for the FGMEE energy harvester calculated by ICS-FEM with 60×4 meshes and FEM with 240×16 meshes are shown in Figure 14. The first eleven natural frequencies calculated by ICS-FEM are closer to the reference solutions than those calculated by FEM, indicating ICS-FEM is more efficient than FEM owing to the reduced number of meshes. The ICS-FEM does not take the derivative of the shape functions of the element and can be much easily generated automatically for complicated domains, thus significantly decreasing the numerical errors. The natural frequencies f_{eq} and $f_{\text{eq-}\Phi\Phi}$ agree well with each other since the piezomagnetic phase is absent from the BaTiO_3 FGMEE energy harvester. Moreover, $f_{\text{eq-re}}$ coincides with f_{eq} of the BaTiO_3 FGMEE energy harvester as the magnetoelectric effect is absent in pure BaTiO_3 materials. The f_{uu} and f_{eq} are very close, so the piezoelectric effect only slightly affects the natural frequencies of the energy harvester, which increase with the rise of the exponential factor.

The Wilson- θ method and the equivalent stiffness matrix $[\mathbf{K}_{\text{eq}}]$ were employed to solve the dynamic response of the FGMEE energy harvester. The parameters were set as time step = 0.005 s, $\theta = 1.4$; without damping; sine-wave transient load with a time period of 2 s; 4 cycles of loading (Figure 15). The dynamic behaviors for the harvester calculated by ICS-FEM with 60×4 meshes and FEM with 240×16 meshes are shown in Figures 16 and 17, respectively. The temporal variations of displacement u_y and electric potential Φ calculated by ICS-FEM are closer to the reference solutions than those by FEM, which validate the accuracy of ICS-FEM. The temporal variations of u_y and Φ of the FGMEE energy harvester decrease with the increase of the exponential factor when the material properties of the harvester are in exponential distribution.

6. Conclusions

The free vibrations on FGMEE structures were studied. Firstly, ICS-FEM for FGMEE materials was formulated by incorporating gradient smoothing into the FEM-based computation for the FGMEE multi-physics field. Then the equations of free vibration computation were deduced for the multi-physics coupling field of FGMEE materials. Finally, the FGMEE beams were calculated with functional gradient exponential form or power law form under different boundary conditions.

(i) ICS-FEM reduced the systematic stiffness of the finite element, which improved the computational accuracy compared with FEM under the same element number. ICS-FEM was more efficient than FEM in terms of computation time for the same accuracy.

(ii) Due to the material property changes in each smoothing element, the true parameters at the Gaussian integration

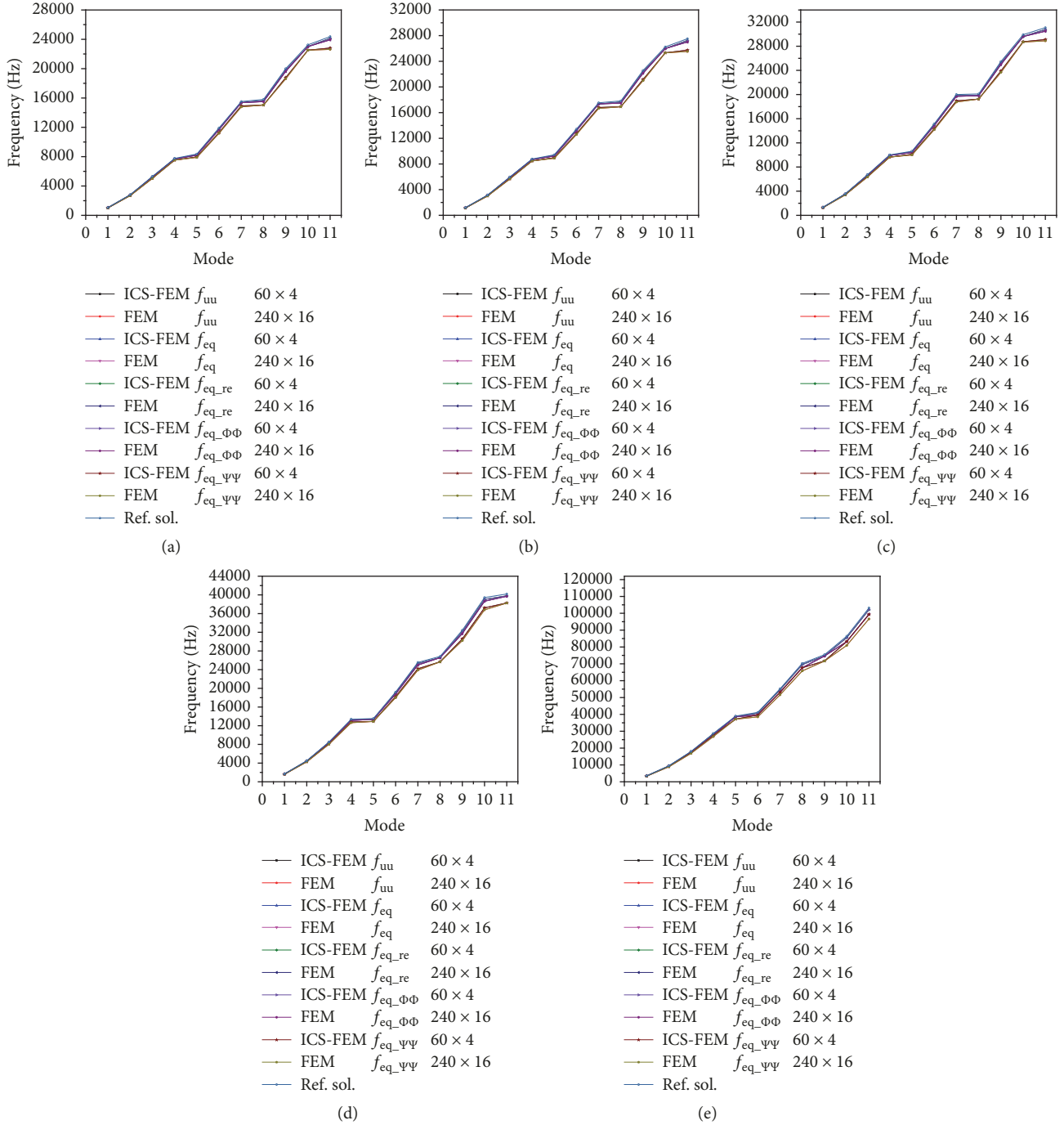


FIGURE 14: Structural frequencies f for BaTiO₃ FGME energy harvester with exponential factor $\eta =$ (a) 0, (b) 0.5, (c) 1.0, (d) 2.0, and (e) 5.0.

point were adopted directly. ICS-FEM avoided the derivative of the shape functions but only transformed the area integral to the boundary integral in the solution domain, which omitted the requirement of continuity of the shape function.

(iii) The magnetic effect slightly influenced the natural frequencies of FGME beams, which increased with the increase of the exponential factor when the material properties of FGME beams were under exponential distribution.

The natural frequency of FGME beams lied in between those of the FGME beams using the bottom surface of materials and the FGME beams using the upper surface, when the material properties of FGME beams were under the power law distribution.

(iv) The natural frequencies and general displacements of the FGME energy harvester developed by ICS-FEM were more accurate compared with FEM, owing to the reduced number of meshes.

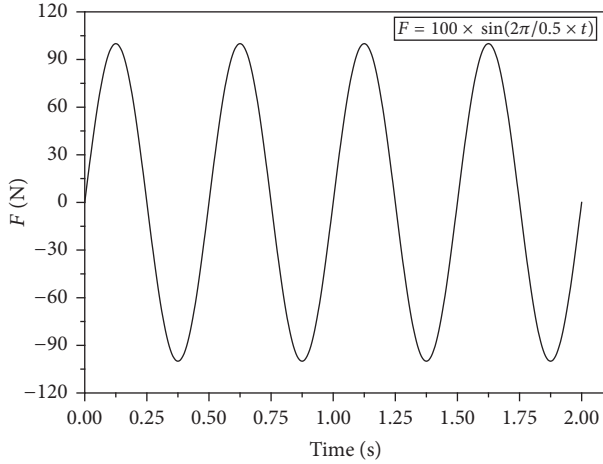


FIGURE 15: Sine-wave load at point A of the BaTiO₃ FGME energy harvester.

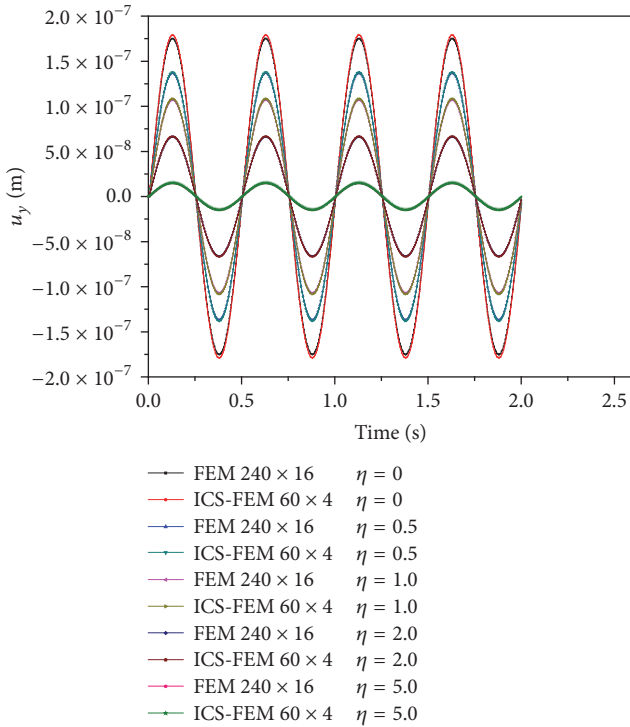


FIGURE 16: Temporal variations of displacement u_y at point B of BaTiO₃ FGME energy harvester with different values of exponential factor calculated by ICS-FEM and FEM.

Conflicts of Interest

The authors declare that they have no conflicts of interest.

Acknowledgments

Special thanks are due to Professor Guirong Liu for the S-FEM Source Code in <http://www.ase.uc.edu/~liugr/software.html>. This work was financially supported by the National Natural Science Foundation of China (Grant

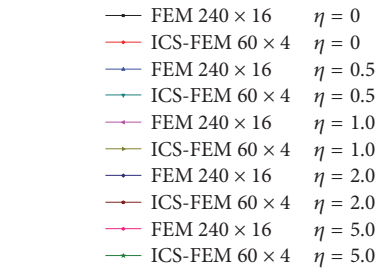
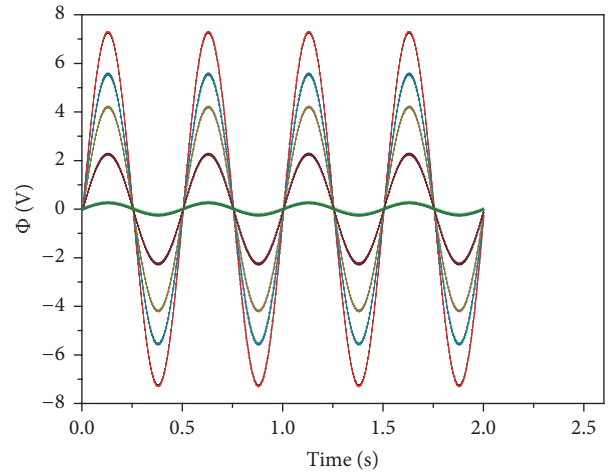


FIGURE 17: Temporal variations of electric potential Φ at point A of BaTiO₃ FGME energy harvester with different values of exponential factor calculated by ICS-FEM and FEM.

no. 11502092), Jilin Provincial Department of Science and Technology Fund Project (Grant nos. 20160520064JH, 20170101043JC), and the Fundamental Research Funds for the Central Universities.

References

- [1] W. Eerenstein, N. D. Mathur, and J. F. Scott, "Multiferroic and magnetoelectric materials," *Nature*, vol. 442, no. 7104, pp. 759–765, 2006.
- [2] J. F. Scott, "Applications of magnetoelectrics," *Journal of Materials Chemistry*, vol. 22, no. 11, pp. 4567–4574, 2012.
- [3] A. Zhang and B. Wang, "Effects of crack surface electrostatic tractions on the fracture behaviour of magnetoelectric composite materials," *Mechanics of Materials*, vol. 102, pp. 15–25, 2016.
- [4] J. Zhai, Z. Xing, S. Dong, J. Li, and D. Viehland, "Detection of pico-Tesla magnetic fields using magneto-electric sensors at room temperature," *Applied Physics Letters*, vol. 88, no. 6, Article ID 062510, 2006.
- [5] D. J. Huang, H. J. Ding, and W. Q. Chen, "Analytical solution for functionally graded magneto-electro-elastic plane beams," *International Journal of Engineering Science*, vol. 45, no. 2-8, pp. 467–485, 2007.
- [6] A. Milazzo, C. Orlando, and A. Alaimo, "An analytical solution for the magneto-electro-elastic bimorph beam forced vibrations problem," *Smart Materials and Structures*, vol. 18, no. 8, Article ID 085012, 2009.

- [7] W. Q. Chen, K. Y. Lee, and H. J. Ding, "On free vibration of non-homogeneous transversely isotropic magneto-electro-elastic plates," *Journal of Sound and Vibration*, vol. 279, no. 1-2, pp. 237–251, 2005.
- [8] C.-P. Wu and Y.-C. Lu, "A modified Pagano method for the 3D dynamic responses of functionally graded magneto-electro-elastic plates," *Composite Structures*, vol. 90, no. 3, pp. 363–372, 2009.
- [9] A. R. Annigeri, N. Ganesan, and S. Swarnamani, "Free vibration behaviour of multiphase and layered magneto-electro-elastic beam," *Journal of Sound and Vibration*, vol. 299, no. 1-2, pp. 44–63, 2007.
- [10] R. K. Bhangale and N. Ganesan, "Static analysis of simply supported functionally graded and layered magneto-electro-elastic plates," *International Journal of Solids and Structures*, vol. 43, no. 10, pp. 3230–3253, 2006.
- [11] R. K. Bhangale and N. Ganesan, "Free vibration studies of simply supported non-homogeneous functionally graded magneto-electro-elastic finite cylindrical shells," *Journal of Sound and Vibration*, vol. 288, no. 1-2, pp. 412–422, 2005.
- [12] R. K. Bhangale and N. Ganesan, "Free vibration of simply supported functionally graded and layered magneto-electro-elastic plates by finite element method," *Journal of Sound and Vibration*, vol. 294, no. 4, pp. 1016–1038, 2006.
- [13] R. G. Lage, C. M. M. Soares, C. A. M. Soares, and J. N. Reddy, "Layerwise partial mixed finite element analysis of magneto-electro-elastic plates," *Computers & Structures*, vol. 82, pp. 1293–1301, 2004.
- [14] S. S. Phoenix, S. K. Satsangi, and B. N. Singh, "Layer-wise modelling of magneto-electro-elastic plates," *Journal of Sound and Vibration*, vol. 324, no. 3-5, pp. 798–815, 2009.
- [15] G. R. Buchanan, "Free vibration of an infinite magneto-electro-elastic cylinder," *Journal of Sound and Vibration*, vol. 268, no. 2, pp. 413–426, 2003.
- [16] J. Sladek, V. Sladek, S. Krahulec, C. S. Chen, and D. L. Young, "Analyses of circular magneto-electro-elastic plates with functionally graded material properties," *Mechanics of Advanced Materials and Structures*, vol. 22, no. 6, pp. 479–489, 2015.
- [17] J. Liu, P. Zhang, G. Lin, W. Wang, and S. Lu, "High order solutions for the magneto-electro-elastic plate with non-uniform materials," *International Journal of Mechanical Sciences*, vol. 115-116, pp. 532–551, 2016.
- [18] L.-L. Ke and Y.-S. Wang, "Free vibration of size-dependent magneto-electro-elastic nanobeams based on the nonlocal theory," *Physica E: Low-Dimensional Systems and Nanostructures*, vol. 63, pp. 52–61, 2014.
- [19] G. R. Liu, H. Nguyen-Xuan, and T. Nguyen-Thoi, "A theoretical study on the smoothed FEM (S-FEM) models: properties, accuracy and convergence rates," *International Journal for Numerical Methods in Engineering*, vol. 84, no. 10, pp. 1222–1256, 2010.
- [20] S. P. Bordas and S. Natarajan, "On the approximation in the smoothed finite element method (SFEM)," *International Journal for Numerical Methods in Engineering*, vol. 81, no. 5, pp. 660–670, 2010.
- [21] G. R. Liu and G. Y. Zhang, "A normed G space and weakened weak (W-2) formulation of a cell-based smoothed point interpolation method," *International Journal of Computational Methods*, vol. 6, no. 1, pp. 147–179, 2009.
- [22] G. R. Liu, T. T. Nguyen, K. Y. Dai, and K. Y. Lam, "Theoretical aspects of the smoothed finite element method (SFEM)," *International Journal for Numerical Methods in Engineering*, vol. 71, no. 8, pp. 902–930, 2007.
- [23] H. Feng, X. Cui, and G. Li, "A stable nodal integration method for static and quasi-static electromagnetic field computation," *Journal of Computational Physics*, vol. 336, pp. 580–594, 2017.
- [24] S. Li, X. Cui, H. Feng, and G. Wang, "An electromagnetic forming analysis modelling using nodal integration axisymmetric thin shell," *Journal of Materials Processing Technology*, vol. 244, pp. 62–72, 2017.
- [25] S. Natarajan, A. J. M. Ferreira, S. P. A. Bordas, E. Carrera, and M. Cinefra, "Analysis of composite plates by a unified formulation-cell based smoothed finite element method and field consistent elements," *Composite Structures*, vol. 105, pp. 75–81, 2013.
- [26] K. Nguyen-Quang, H. Dang-Trung, V. Ho-Huu, H. Luong-Van, and T. Nguyen-Thoi, "Analysis and control of FGM plates integrated with piezoelectric sensors and actuators using cell-based smoothed discrete shear gap method (CS-DSG3)," *Composite Structures*, vol. 165, pp. 115–129, 2017.
- [27] T. Nguyen-Thoi, H. C. Vu-Do, T. Rabczuk, and H. Nguyen-Xuan, "A node-based smoothed finite element method (NS-FEM) for upper bound solution to visco-elastoplastic analyses of solids using triangular and tetrahedral meshes," *Computer Methods Applied Mechanics and Engineering*, vol. 199, no. 45-48, pp. 3005–3027, 2010.
- [28] T. Nguyen-Thoi, G. R. Liu, H. Nguyen-Xuan, and C. Nguyen-Tran, "Adaptive analysis using the node-based smoothed finite element method (NS-FEM)," *International Journal for Numerical Methods in Biomedical Engineering*, vol. 27, no. 2, pp. 198–218, 2011.
- [29] T. N. Tran, G. R. Liu, H. Nguyen-Xuan, and T. Nguyen-Thoi, "An edge-based smoothed finite element method for primal-dual shakedown analysis of structures," *International Journal for Numerical Methods in Engineering*, vol. 82, no. 7, pp. 917–938, 2010.
- [30] H. Nguyen-Xuan, L. V. Tran, T. Nguyen-Thoi, and H. C. Vu-Do, "Analysis of functionally graded plates using an edge-based smoothed finite element method," *Composite Structures*, vol. 93, no. 11, pp. 3019–3039, 2011.
- [31] W. Li, Y. Chai, M. Lei, and G. R. Liu, "Analysis of coupled structural-acoustic problems based on the smoothed finite element method (S-FEM)," *Engineering Analysis with Boundary Elements*, vol. 42, pp. 84–91, 2014.
- [32] T. Nguyen-Thoi, G. R. Liu, H. C. Vu-Do, and H. Nguyen-Xuan, "A face-based smoothed finite element method (FS-FEM) for visco-elastoplastic analyses of 3D solids using tetrahedral mesh," *Computer Methods Applied Mechanics and Engineering*, vol. 198, no. 41-44, pp. 3479–3498, 2009.
- [33] C. Jiang, Z.-Q. Zhang, G. R. Liu, X. Han, and W. Zeng, "An edge-based/node-based selective smoothed finite element method using tetrahedrons for cardiovascular tissues," *Engineering Analysis with Boundary Elements*, vol. 59, pp. 62–77, 2015.
- [34] W. Zeng, G. R. Liu, D. Li, and X. W. Dong, "A smoothing technique based beta finite element method (beta FEM) for crystal plasticity modeling," *Computers & Structures*, vol. 162, pp. 48–67, 2016.
- [35] H. Nguyen-Van, N. Mai-Duy, and T. Tran-Cong, "A smoothed four-node piezoelectric element for analysis of two-dimensional smart structures," *Computer Modeling in Engineering and Sciences*, vol. 23, no. 3, pp. 209–222, 2008.
- [36] Y. Onishi, R. Iida, and K. Amaya, "F-bar aided edge-based smoothed finite element method using tetrahedral elements for finite deformation analysis of nearly incompressible solids,"

- International Journal for Numerical Methods in Engineering*, vol. 109, no. 11, pp. 1582–1606, 2017.
- [37] W. Zuo and K. Saitou, “Multi-material topology optimization using ordered SIMP interpolation,” *Structural and Multidisciplinary Optimization*, vol. 55, no. 2, pp. 477–491, 2017.
- [38] L. M. Zhou, G. W. Meng, F. Li, and H. Wang, “Cell-based smoothed finite element method-virtual crack closure technique for a piezoelectric material of crack,” *Mathematical Problems in Engineering*, vol. 2015, Article ID 371083, 10 pages, 2015.
- [39] C. V. Le, “Estimation of bearing capacity factors of cohesive-frictional soil using the cell-based smoothed finite element method,” *Computers & Geosciences*, vol. 83, pp. 178–183, 2017.
- [40] L. M. Zhou, G. W. Meng, F. Li, and S. Gu, “A cell-based smoothed XFEM for fracture in piezoelectric materials,” *Advances in Materials Science and Engineering*, vol. 2016, Article ID 4125307, 14 pages, 2016.
- [41] A. L. Pramod, S. Natarajan, A. J. Ferreira, E. Carrera, and M. Cinefra, “Static and free vibration analysis of cross-ply laminated plates using the Reissner-mixed variational theorem and the cell based smoothed finite element method,” *European Journal of Mechanics-A/Solids*, vol. 62, pp. 14–21, 2017.
- [42] F. Wu, L. Y. Yao, M. Hu, and Z. C. He, “A stochastic perturbation edge-based smoothed finite element method for the analysis of uncertain structural-acoustics problems with random variables,” *Engineering Analysis with Boundary Elements*, vol. 80, pp. 116–126, 2017.
- [43] J. L. Mantari, E. M. Bonilla, and C. Guedes Soares, “A new tangential-exponential higher order shear deformation theory for advanced composite plates,” *Composites Part B: Engineering*, vol. 60, pp. 319–328, 2014.
- [44] A. Daga, N. Ganesan, and K. Shankar, “Behaviour of magneto-electro-elastic sensors under transient mechanical loading,” *Sensors and Actuators A: Physical*, vol. 150, no. 1, pp. 46–55, 2009.

